Diagrammatic many-body perturbation theory applied to highly ionized atoms of the copper isoelectronic sequence

S. M. Younger

National Measurement Laboratory, National Bureau of Standards, Washington, D. C. 20234
(Received 8 February 1979)

Many-body diagrammatic perturbation theory has been applied to the calculation of ionization energies and multiplet strengths for two highly ionized atoms of the copper isoelectronic sequence. A unified Hartree-Fock zeroth-order Hamiltonian the eigenfunctions of which include both open- and closed-shell orbitals has been constructed for systems with a single open shell. Correlation energies for the excited $4p$ states as well as the ground $4s$ states of Kr VIII and Mo XIV were computed by means of individual basis sets generated for each state. The distribution of the $3l$-$4l'$ correlation energy among second- and higher-order terms differed significantly for the two ions. In Mo XIV, most of the correlation energy was concentrated in second-order, with small third-order effects. In Kr VIII, however, second-order results were substantially changed by higher-order diagrams, particularly in the case of the $4p$ state. Correlated multiplet strengths for the $4s\,^2S$-$4p\,^2P$ resonance transition were computed, including first-order corrections to the Hartree-Fock zeroth-order wave functions for both initial and final states. The results of these calculations are in excellent agreement with those of recent multiconfiguration Hartree-Fock calculations.

I. INTRODUCTION

The rapid development of plasma physics, both laboratory and astrophysical, has created a renewed interest in the accurate calculation of the properties of highly charged ions.[1,2] In tokamaks, for example, it has been found that trace amounts of heavy-ion impurities in the plasma lead to substantial radiant energy loss.[3] Thus, a knowledge of the transition probabilities and wavelengths of reactor wall materials is of great importance in the design and diagnostics of plasma fusion machines. The interpretation of recent spectra from solar flares and other highly energetic astrophysical events also demands accurate atomic data.

The beam-foil technique[4] is currently the only available experimental method for the generation and observation of such highly ionized species. In the past several years, however, a systematic discrepancy between experimental transition probabilities determined by the beam-foil method and theoretical data has been recognized.[3,5] This discrepancy has been found to be most serious for heavy isoelectronic sequences, exceeding 30% for most ions of the copper sequence, and has been interpreted by Younger and Wiese[6] as due to masking cascades in the observed decays. As a result of this serious experimental problem, renewed emphasis has been placed on theoretical methods for the accurate calculation of spectral data.

Almost all accurate calculations of transition probabilities have been performed using some form of multiconfiguration Hartree-Fock (MCHF) or superposition-of-configuration method. Given the serious discrepancies reported between such theoretical data and those from beam-foil experiments, however, it has become desirable to investigate an alternate method, based on a different formal scheme, which may serve as a check on these methods.

Kelly has developed the formal aspects of Bruckner-Goldstone perturbation theory[7] applied to atoms and has made extensive calculations of atomic properties using "diagrammatic perturbation theory." We will use this perturbative approach, suitably modified for the open-shell case, for an independent study of the copper sequence correlation problem. The computational procedures which will be used in the present work follow those outlined in an excellent review of many-body perturbation theory by Kelly.[8]

II. ZEROTH-ORDER HAMILTONIAN

The choice of the zeroth-order or "model" Hamiltonian is of great importance in constructing the perturbation expansion, for although in principle many fulfill the general requirements (e.g., Hartree-Fock, Thomas-Fermi, statistical exchange, hydrogenic, etc.), the amount of labor involved in achieving a desired accuracy will depend on how close H_0 is to the exact Hamiltonian, that is, the magnitude of the perturbation.

For a closed-shell system, the Hartree-Fock Hamiltonian H_0^{HF} is given by

$$H_0^{\text{HF}} = t + \sum_{i=1}^{N_T} (2J_i - K_i), \tag{1}$$

where t is the "bare nuclear" term, including the kinetic energy and the nuclear attraction, and J_i and K_i are the direct and exchange electrostatic operators.[9] The sum is over the total number of electrons, N_T, in the atom. The set $\{\phi_i\}$ of all solutions to Eq. (1) corresponding to occupied single-particle states is invariant with respect to unitary transformations, a fact which allows the eigenvalue matrix to be diagonalized.

For a closed-shell system, one can then define a single operator H_0^{HF} which has as its eigenfunctions a set of N occupied orbitals (the usual Hartree-Fock orbitals for an atom) and an infinite set of unoccupied or virtual orbitals.

For open-shell atoms, the situation is somewhat more complicated in that the usual Hartree-Fock equation describing the closed-shell core states is different from the one describing the open shell. Since the perturbation formalism requires a *single* zeroth-order equation which generates all occupied and virtual orbitals, a method must be devised to combine the two sets of equations into a unified Hamiltonian having both open- and closed-shell eigenfunctions.

Roothaan,[9] in his investigations of self-consistent-field theory for open-shell atoms, found that such a "unified" Hartree-Fock Hamiltonian may be defined by the use of coupling operators. Let $\bar{\phi}_i$ represent the set of doubly occupied (i.e., spin-degenerate) closed-shell orbitals, and $\bar{\phi}_0$ the set of all possible open-shell orbitals of the chosen principal quantum number and angular momentum. In the following we assume a single open shell. Following Roothaan's notation, let the subscripts k and l correspond to closed-shell orbitals, m to open-shell orbitals, and i and j to orbitals of either set. Define the direct, L_i, and exchange-, M_i, coupling operators as

$$L_i \phi = \langle \phi_i | J_0 | \phi \rangle \phi_i + \langle \phi_i | \phi \rangle J_0 \phi_i \,,$$

and   (2)

$$M_i \phi = \langle \phi_i | K_0 | \phi \rangle \phi_i + \langle \phi_i | \phi \rangle K_0 \phi_i \,.$$

The total open- and closed-shell electrostatic operators are

$$J_0 = f \sum_m J_m, \quad J_c = \sum_k J_k, \quad J_T = J_c + J_0 \,,$$

$$K_0 = f \sum_m K_m, \quad K_c = \sum_k K_k, \quad K_T = K_c + K_0 \,. \tag{3}$$

In Eq. (3), f is the fractional occupation number of the open shell, i.e., the number of occupied open-shell states over the total number of all possible open-shell states. The total direct and exchange coupling operators are similarly defined:

$$L_0 = f \sum_m L_m, \quad L_c = \sum_k L_k, \quad L_T = L_c + L_0 \,,$$

$$M_0 = f \sum_m M_m, \quad M_c = \sum_k M_k, \quad M_T = M_c + M_0 \,. \tag{4}$$

The desired unified Hartree-Fock Hamiltonian then has the form

$$F = t + (2J_T - K_T) + 2\alpha (L_T - J_0) - \beta (M_T - K_0) \,, \tag{5}$$

where α and β are constants depending on the angular momentum of the open-shell state. For one electron outside a closed-shell core

$$\alpha = \beta = 1/(1 - f)$$

and   (6)

$$f = 1/2(2l + 1) \,.$$

There are three sets of eigenfunctions associated with the operator F: closed shell, open shell, and virtual. Each of these will be considered in turn. A simple example is discussed in the Appendix.

(a) Closed shell orbitals. Consider F acting on a closed-shell core orbital ϕ_j:

$$F\phi_j = t\phi_j + (2J_T - K_T)\phi_j$$

$$+ \frac{1}{1-f} \sum_k [\langle \phi_k | 2J_0 - K_0 | \phi_j \rangle \phi_k \delta_{l_k,l_j} \delta_{m_k,m_j}]$$

$$+ \frac{f}{1-f} \sum_m [\langle \phi_m | 2J_0 - K_0 | \phi_j \rangle \phi_m \delta_{l_m,l_j} \delta_{m_m,m_j}] \,,$$

$$\tag{7}$$

where l_j and m_j are angular and magnetic quantum numbers. Note that the orbitals $\bar{\phi}_0$ and $\bar{\phi}_c$ are already defined as solutions of the usual Hartree-Fock problem. The matrix $\bar{\epsilon} = \langle \bar{\phi}_c | F | \bar{\phi}_c \rangle$ may then be computed using these known orbitals, and diagonalized to obtain the closed-shell eigenfunctions of F.

It was found that although the eigenvalues of F are significantly different from those associated with the usual Hartree-Fock orbitals, the mixing of the old Hartree-Fock orbitals to produce unified ones is very slight.

Since in all cases the eigenvalues of F are less than the original Hartree-Fock values, their effect on the perturbation expansion is to reduce the denominators, causing an increase in the value of each diagram. This apparent increase is somewhat misleading, however, in that there exists a a class of higher-order diagrams which exactly cancel the effects of the eigenvalue shift. Consider the diagrams shown in Fig. 1. As hole-pair diagrams, all three are diagonal in the closed-shell hole line p. Their sum equals the product of the corresponding second-order diagram $(\langle pn | v | kk' \rangle |^2/d)$ and the factor
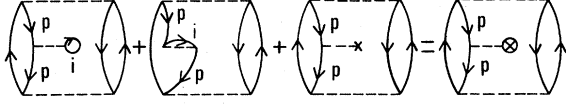
FIG. 1. Third-order diagrams illustrating single-particle insertions on a hole line.

$$\frac{\Delta}{d} = \left(\langle p | V | p \rangle - \sum_{i}^{N_T} [\langle pi | v | pi \rangle - \langle pi | v | ip \rangle] \right) / d , \quad (8)$$

where $d = \epsilon_p + \epsilon_n - \epsilon_k - \epsilon_{k'}$, and where the sum is over the electrons in the atom. V is the potential in F, and k and k' are virtual states. In still higher orders, there are diagrams with two or more single-particle insertions of the type shown in Fig. 1, each insertion contributing a factor of Δ/d. The summation of all such diagrams to all orders is the geometric series

$$\Delta E = \sum_{m} \left(\frac{\Delta}{d} \right)^m \frac{| \langle pn | v | kk' \rangle |^2}{d} \quad (9)$$

or

$$\Delta E = | \langle pn | v | kk' \rangle |^2 (d - \Delta) . \quad (10)$$

Summing from $m = 0$ includes the second-order diagram. The summation of all such single-particle insertions on closed-shell hole lines is accomplished by modifying the denominator of the corresponding second-order diagram.

It is convenient to express the sum in Eq. (10) in terms of the electrostatic operators J and K, so that

$$\Delta = \langle p | V | p \rangle - \sum_{i}^{N_T} \langle p | 2J_i - K_i | p \rangle . \quad (11)$$

For closed-shell core states the matrix element of the single-particle potential is

$$\langle p | V | p \rangle = \langle p | 2J_T - K_T | p \rangle + \frac{1}{1-f} \langle p | 2J_0 - K_0 | p \rangle \quad (12)$$

so that

$$\Delta = [1/(1-f)] \langle p | 2J_0 - K_0 | p \rangle . \quad (13)$$

The denominator shift Δ is identical to the difference between the original Hartree-Fock eigenvalue and the eigenvalue of F, that is

$$\epsilon_F = \langle p | t | p \rangle + \langle p | 2J_T - K_T | p \rangle + \frac{1}{1-f} \langle p | 2J_0 - K_0 | p \rangle , \quad (14)$$

so that

$$\epsilon_F = \epsilon_{HF} + \Delta .$$

One may evaluate the sum of all higher-order single-particle insertions on hole lines by simply using the original Hartree-Fock eigenvalues in the second-order energy denominator, thereby eliminating the need for explicitly calculating such diagrams. In the present calculations, all denominators are assumed to be formed from the original Hartree-Fock hole eigenvalues.

(b) Open shell orbitals. F acting on an open-shell orbital produces

$$F\phi_0 = t\phi_0 + (2J_c - K_c)\phi_0 + \frac{1}{1-f} \sum_{j} \langle \phi_j | 2J_0 - K_0 | \phi_0 \rangle \phi_j$$
$$+ [f/(1-f)] \langle \phi_0 | J_0 | \phi_0 \rangle \phi_0 . \quad (15)$$

The open-shell eigenvalue is

$$\epsilon_0 = \langle \phi_0 | t | \phi_0 \rangle + \langle \phi_0 | 2J_c - K_c | \phi_0 \rangle + \frac{f}{1-f} \langle \phi_0 | J_0 | \phi_0 \rangle \quad (16)$$

which is equivalent to

$$\epsilon_0 = \epsilon_0^{HF} + [f/(1-f)] \langle \phi_0 | J_0 | \phi_0 \rangle . \quad (17)$$

Since there is no coupling of open- and closed-shell orbitals, the eigenfunction of the original Hartree-Fock problem for the open shell is also the eigenfunction of F. The eigenvalue is shifted upward by an amount $[f/(1-f)] \langle \phi_0 | J_0 | \phi_0 \rangle$ decreasing the value of the denominators and increasing the value of each diagram in which it occurs. Again the consideration of higher-order diagrams containing single-particle insertions on the open-shell hole line is equivalent to a shift in the second-order energy denominator, which is equal to the shift caused by the transformation to the unified Hamiltonian.

(c) Virtual orbitals. In addition to the set of N occupied eigenfunctions, the operator F also has associated with it an infinite set of unoccupied orbitals or "excited" single-particle states (not to be confused with the physical excited states of the system). F acting on such an orbital yields

$$F\phi_v = t\phi_v + (2J_T - K_T)\phi_v - \frac{1}{1-f}(2J_0 - K_0)\phi_v$$
$$+ \sum_{j} \frac{1}{1-f} \langle \phi_j | 2J_0 - K_0 | \phi_v \rangle \phi_j$$
$$+ \frac{f}{1-f} \sum_{m} \langle \phi_m | 2J_0 - K_0 | \phi_v \rangle \phi_m \quad (18)$$

or

$$F\phi_v = t\phi_v + (2J_c - K_c)\phi_v - \frac{f}{1-f}(2J_0 - K_0)\phi_v$$
$$+ \frac{1}{1-f} \sum_{j} \langle \phi_j | 2J_0 - K_0 | \phi_v \rangle \phi_j \delta_{l_j l_v} \delta_{m_j m_v}$$
$$+ \frac{f}{1-f} \sum_{m} \langle \phi_m | 2J_0 - K_0 | \phi_0 \rangle \phi_m \delta_{l_m l_v} \delta_{m_0 m_v} . \quad (19)$$

The presence of the coupling operator in F results in a complex potential for the virtual-state calculations. Consider the asymptotic form of F in the limit of large radii. As $r \to \infty$, $K_i \to 0$ since ϕ_i, an occupied orbital, tends to zero at infinity faster than r^{-1}. Also as $r \to \infty$, $J_i \to 1/r$ reflecting the nuclear screening effects of the occupied orbitals. Then as $r \to \infty$, the left-hand side of Eq. (19) becomes

$$F\phi_v \to t\phi_v + \frac{N_c}{r}\phi_v - \frac{f}{1-f}\frac{1}{r}\phi_v$$

$$= t\phi_v + \left(N_c - \frac{f}{1-f}\right)\frac{1}{r}\phi_v . \qquad (20)$$

The asymptotic charge seen by the virtual orbital of the unified Hamiltonian is greater than that seen by the physical excited states of the atom. For lower excited states the decreased screening is partially balanced by the presence of the coupled core-state functions in the Hamiltonian. The first few bound states have maxima quite close to the core, substantially penetrating the core orbitals. The effect of the coupling operators in mixing the core functions with the virtual state is to negate to some degree the change in asymptotic charge. For example, the Hartree-Fock "physical" $4p$ excited state of Kr VIII is almost identical to the virtual $4p$ orbital of the unified operator constructed for the ground-state occupied orbitals. The eigenvalues, however, are appreciably different.

III. IONIZATION ENERGIES

A. Experimental

For the Cu-sequence energy levels studied here, the ionization energy is that of a single $n = 4$ electron outside a closed-shell

$$1s^2 2s^2 2p^6 3s^2 3p^6 3d^{10} {}^1S_0$$

core. The correlation contribution to the ionization energy is defined as

$$I_{corr} = I - I_{HF} , \qquad (21)$$

where I is the exact nonrelativistic ionization energy (the observed energy minus the relativistic contribution) and I_{HF} is the corresponding Hartree-Fock value. Accurate ionization potentials for Kr VIII and Mo XIV have been derived from spectral observations by Reader.[10]

In order to obtain nonrelativistic ionization energies, it is necessary to subtract from the observed values the contributions due to relativistic effects. Relativistic shifts and spin-orbit parameters have been calculated by Weiss[11] using the one-electron Pauli approximation with Hartree-Fock wave func-

tions.

In Table I, we list Reader's experimentally derived ionization energies, the relativistic shifts of Weiss, the resulting nonrelativistic ionization energies, and the ionization correlation energies. Theoretical nonrelativistic ionization energies have been reported for Kr VIII by Froese-Fischer[12] using the MCHF method, with the following results: Kr VIII $4s$ 4.560 and $4p$ 3.914 a.u.

B. Many-body perturbation-theory ionization energies

The correlation energy of the

$$1s^2 2s^2 2p^6 3s^2 3p^6 3d^{10} 4l$$

state of Cu-like ions may be divided into two components: one describing correlation within the core, and the other the interaction of the $4l$ electron with the core:

$$E_{corr} = E_{core} + E_{4l-core} . \qquad (22)$$

The correlation correction to the ionization energy is the difference of the total correlation energies before and after ionization:

$$I_{corr} = E_{corr}(N-1) - E_{corr}(N) . \qquad (23)$$

For a single electron outside a closed-shell core consisting entirely of subshells of lower principal quantum numbers than the optical electron, core-correlation effects should remain constant to a good approximation before and after ionization, i.e.,

$$E_{corr}(N-1) \approx E_{core}(N) , \qquad (24)$$

so that I_{corr} is simply $E_{4l-core}$. The core wave functions for 29- and 28-electron Kr and Mo are almost identical for both the $4s$ and $4p$ states, which further support this assumption. Thus, the only diagrams which will be considered here are those containing both $4l$ and core hole lines.

(a) Second-order diagrams. The only nonvanishing second-order energy diagrams associated with the unified Hamiltonian described in Sec. II are

TABLE I. Experimental ionization energies (a.u.).

		I_{obs} [a]	I_{rel} [b]	I_{obs}^{nonrel} [c]	I_{obs}^{corr} [d]
$4s$	Kr VIII	4.622	−0.066	4.556	−0.042
	Mo XIV	11.120	−0.205	10.915	−0.044
$4p$	Kr VIII	3.947	−0.020	3.927	−0.044
	Mo XIV	9.948	−0.072	0.876	−0.039

[a] I_{obs}: observed ionization energy (Ref. 10).
[b] I_{rel}: relativistic shift (Weiss) (Ref. 11).
[c] I_{obs}^{nonrel}: nonrelativistic ionization energy.
[d] I_{obs}^{corr}: observed correlation energy.

the direct and exchange pair diagrams. That there are no surviving single-particle diagrams in second order is due to the cancellation of the first-order single-particle contribution to the wave function for this Hamiltonian. To illustrate this, let V represent the potential in the unified Hamiltonian. Then the single-particle correction to the $4l$ state involving a single excitation to the virtual state $|k\rangle$ is

$$\eta = \frac{1}{\epsilon_{4l} - \epsilon_k} \sum_{i \neq 4l}^{N_T} \{[\langle 4li|v|ki\rangle - \langle 4li|v|ik\rangle]$$
$$- \langle 4l|V|k\rangle\}|k\rangle . \tag{25}$$

Evaluating the matrix element V,

$$\eta = \frac{1}{\epsilon_{4l} - \epsilon_k} \sum_{i \neq 4l}^{N_T} \{[4li|v|ki\rangle - \langle 4li|v|ik\rangle]$$
$$- \langle 4l|2J_T - K_T|k\rangle$$
$$+ \langle 4l|2J_0 - K_0|k\rangle\}|k\rangle$$
$$= 0 . \tag{26}$$

It follows then that the single-particle correlation-energy diagrams also cancel, leaving only the pair diagrams in second order.

The basis states used to construct the pair diagrams are those virtual orbitals corresponding to the unified Hamiltonians for the $4s$ and $4p$ states. Numerical solutions to the radial Schrödinger equation were obtained using the author's Hartree-Fock program. Five to ten bound states and 20 to 30 continuum orbitals in the range $k = 0-10$ a.u. were found adequate to describe correlation effects.

Completely separate sets are required for the $4s$ and $4p$ correlations because of the difference in the Hamiltonians defining each. The techniques for the summation over the excited states of the diagrams are those of Kelly.[8]

Numerical values for the second-order pair diagrams are given in Table II for the $4s$ states and Table III for the $4p$ states of Kr VIII and Mo XIV. Tabulated are all diagrams with nonzero angular factors. As expected, the largest correlations are between the $4l$ electron and the $3d^{10}$ subshell. The closeness of the $4l$ to the $3d$, as well as the large population of the latter, makes this reasonable. Progressively smaller effects are observed for the $3p$ and $3s$ subshells, because of their smaller populations and the larger eigenvalues they contribute to diagram denominators. Correlation between the $4l$ electron and $n = 1$ or $n = 2$ orbitals is expected to be extremely small since the wave functions overlap only deep within the core where the $4l$ function is small. The large eigenvalues associated with the core orbitals produce large energy denominators which further reduce the value of diagrams containing such inner-shell lines.

The exchange diagrams are generally much smaller than the direct diagrams. The largest direct diagrams were found to be those involving one bound and one continuum excitation. Next largest were continuum-continuum diagrams with bound-bound contributions least. It is not possible then to estimate the importance of a particular diagram merely by examining a few bound-bound diagrams alone. It is quite possible that bound-bound

TABLE II. $4s$ second-order correlation energies ($\times 10^{-3}$ a.u.).

	Kr VIII		Mo XIV	
Excitation pair	Direct	Exchange	Direct	Exchange
$3d4s \rightarrow kpk'p$	−2.554	0.403	−1.39	0.16
$kfk'p$	−34.574	2.078	−36.76	1.96
$kpk'f$	−0.811	2.078	−0.65	1.96
$kfk'f$	−1.225	0.405	−1.24	0.50
$kdk's$	−13.984	−0.244	−8.30	0.47
$ksk'd$	−0.410	−0.244	−0.09	0.47
$kdk'd$	−0.470	1.200	−0.56	0.10
Total $3d4s$:	−54.029	4.597	−48.99	5.62
$3p4s \rightarrow kpk's$	−4.439	−0.071	−5.00	0.14
$ksk'p$	−0.390	−0.071	−0.26	0.14
$kfk'd$	−3.296	0.411	−4.17	0.68
$kdk'f$	−0.377	0.411	−0.48	0.68
$kdk'p$	−1.544	−0.042	−2.54	0.04
$kpk'd$	−0.246	−0.042	−0.32	0.04
Total $3p4s$:	−10.293	0.598	−12.77	1.72
$3s4s \rightarrow ksk's$	−1.269	0.547	−0.90	0.40
$kpk'p$	−0.364	−0.036	−0.51	−0.01
$kdk'd$	−0.221	−0.008	−0.47	0.02
$kfk'f$	−0.542	0.193	−0.73	0.26
Total $3s4s$:	−2.395	0.695	−2.61	0.67

TABLE III. $4p$ second-order correlation energies ($\times 10^{-3}$ a.u.).

Excitation pair	Kr VIII Direct	Kr VIII Exchange	Mo XIV Direct	Mo XIV Exchange
$3d4p \rightarrow kdk'p$	−20.159	0.356	−7.21	0.01
$kpk'd$	−0.961	0.356	−0.56	0.01
$kdk'f$	−2.867	4.010	−2.67	4.52
$kfk'd$	−4.624	4.010	−5.20	4.52
$ksk'p$	−0.252	0.030	−0.54	0.01
$kpk's$	−0.741	0.030	−0.46	0.01
$ksk'f$	−0.644	1.026	−0.51	0.96
$kfk's$	−11.285	1.026	−11.79	0.96
Total $3d\,4p$:	−41.533	10.844	−28.92	11.01
$3p4p \rightarrow kpk'p$	−7.369	1.094	−3.28	0.43
$kdk'd$	−1.364	0.089	−1.67	0.05
$kfk'f$	−1.599	0.168	−2.09	0.23
$ksk's$	−0.196	0.072	−0.20	0.03
$ksk'd$	−0.221	0.018	−0.26	0.01
$kdk's$	−0.766	0.018	−0.88	0.01
$kpk'f$	−0.269	0.128	−0.33	0.11
$kfk'p$	−1.037	0.128	−1.18	0.11
Total $3p4p$:	−12.821	1.715	−9.99	0.97
$3s4p \rightarrow kpk'd$	−0.110	0.003	−0.22	0.02
$kdk'p$	−0.097	0.003	−0.13	0.02
$kdk'f$	−0.223	0.068	−0.34	0.10
$kfk'd$	−0.198	0.068	−0.30	0.10
$ksk'p$	−2.106	0.155	−0.63	0.03
$kpk's$	−0.086	0.155	−0.10	0.03
Total $3s4p$:	−2.820	0.452	−1.71	0.29

diagrams are small while continuum-bound or continuum-continuum diagrams are large.

For the $4s$ state, most of the correlation results from the excitations $3d4s \rightarrow kdk's, \rightarrow kfk'p, \rightarrow kpk'p$ and $3p4s \rightarrow kpk's, \rightarrow kfk'd$. Although the relative importance of the excitations differ for Kr and Mo, these five diagrams contribute over 85% of the second-order direct correlation. For the $4p$ state, the most important diagrams involved excitations of the kind $3d4p \rightarrow kdk'p, \rightarrow kfk's$ and $3p4p \rightarrow kpk'p, \rightarrow kdk'd, \rightarrow kfk'f$.

Included in Tables II and III are diagrams involving the excitation of a $3l$ electron into an unoccupied $4l$ state, e.g., $4s^+3d^- \rightarrow kd4s^-$. The magnitudes of these diagrams were only a few percent of the total correlation energies, mainly due to small angular factors.

In all of the diagrams discussed in this section and Sec. IV, we have employed the original Hartree-Fock (i.e., nonunified) eigenvalues in computing the energy denominators, as discussed in Sec. II. Technically, therefore, these diagrams contain higher-order single-particle insertions on the hole lines, effectively counteracting an artifact produced by the unification of the Fock operators for the open and closed shells.

(b) *Third-order diagrams*. Third-order diagrams corresponding to the unified Hamiltonian, in which there are no single-particle excitations, are shown in Fig. 2. The presence of three interaction lines, along with the triple summation over excited states, makes the evaluation of these dia-
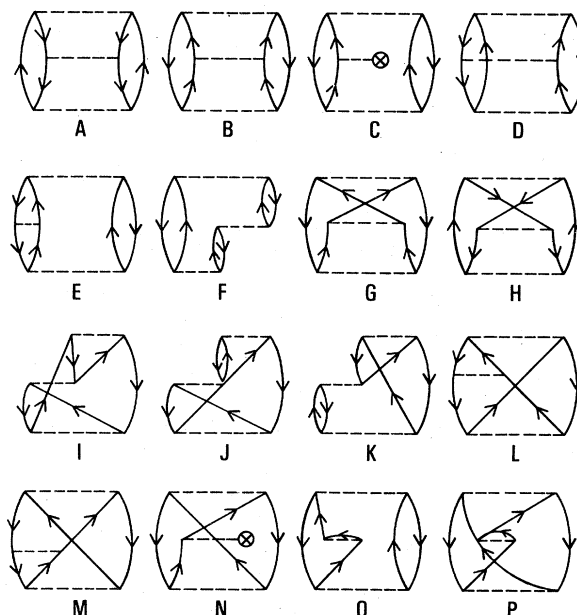
FIG. 2. Third-order correlation energy diagrams.

grams much more difficult than their second-order counterparts. Because of the expected convergent nature of the perturbation series, however, and the small magnitude of most second-order excitation pairs (arising from small radial matrix elements which also occur in third order), many of these third-order diagrams are small.

For correlation in the $4s$ state, the second-order diagrams $3d4s \rightarrow kdk's, \rightarrow kfk'p$ were the largest. Angular factors and matrix elements are also large for third-order diagrams containing these excitations, so that one might expect sizable third-order results. Exchange diagrams in third order, including Figs. 2(g) and 2(h), comprise products of matrix elements found to be small in the second-order calculations. Since they do not have large angular factors in third order, and contain an additional denominator to further reduce the second-order product, they are expected to be quite small compared even to other "direct" third-order diagrams. Note that the hole-particle diagrams should be included, even though they are exchanges of the ring diagram. The angular factors and matrix elements are large for these diagrams compared to other "exchange" diagrams.

The single-particle insertion diagram shown in Fig. 2(c) is particularly interesting and deserves special attention. For the unified Hamiltonian such a diagram involving correlation between hole states p and q is

$$\Delta E(2c) = \sum_i^{N_T} \frac{\langle pq|v|kk''\rangle}{\epsilon_p + \epsilon_q - \epsilon_k - \epsilon_{k''}}$$

$$[\langle ki|v|k'i\rangle - \langle ki|v|ik'\rangle - \langle k|V|k'\rangle]$$

$$\times \frac{\langle k'k''|v|pq\rangle}{\epsilon_p + \epsilon_q - \epsilon_{k'} - \epsilon_{k''}} . \qquad (27)$$

The factor in square brackets is

$$\sum_i^{N_T} [\quad] = \frac{1}{1-f} \langle k|2J_0 - K_0|k'\rangle , \qquad (28)$$

so that

$$\Delta E(2c) = \frac{1}{1-f} \frac{\langle pq|v|kk''\rangle}{\epsilon_p + \epsilon_q - \epsilon_k - \epsilon_{k''}} \langle k|2J_0 - K_0|k'\rangle$$

$$\times \frac{\langle k'k''|v|pq\rangle}{\epsilon_p + \epsilon_q - \epsilon_k - \epsilon_{k''}} . \qquad (29)$$

Diagrammatically, a single-particle insertion on a particle line is equivalent to a sum of hole-particle diagrams. Note that the coefficients in the sum are dependent on the occupation fraction of the open shell. In a one-electron system, this reduces to a dependence on the open-shell symmetry.

The magnitudes of third-order diagrams for the $4s$ correlation energy are given in Table IV. Individual hole-particle and ring diagrams are illustrated in Fig. 3. Similar diagrams for the $4p$ state, including the important excitation pairs $3d4p \rightarrow kdk'p, \rightarrow kfk's$ are given in Table V. The hole-hole, particle-particle, and ring diagrams are positive, while the hole-particle diagrams are negative.

An important result of these calculations is that in most cases the third-order effects decrease in magnitude with the increasing charge of the ion. For Kr VIII, third-order effects reduce the second-order result by 27%, while in Mo XIV, the third-order contribution reduces the second-order result by about 18%. An even larger effect is seen for the $4p$ state. For Mo XIV, the second-order direct diagram is much smaller than that of Kr VIII. The difference is not recovered until third order, after which the final correlations become comparable. Note that the true extent of the correlation as exhibited in the final (second plus higher orders) correlation energy does not change

TABLE IV. $4s$ third-order correlation energies ($\times 10^{-3}$ a.u.).

Diagram		Kr VIII		Mo XIV	
		$3d4s \rightarrow kdk's$	$3d4s \rightarrow kfk'p$	$3d4s \rightarrow kdk's$	$3d4s \rightarrow kfk'p$
Hole-hole		0.92	2.70	0.33	2.46
	A	−1.96	−2.52	−0.44	−2.34
Hole-particle[a]	B	−1.32	−4.86	−0.57	−4.30
	C	−2.09	−3.64	−0.39	−3.00
	D	−1.45	−3.46	−0.62	−3.24
Particle-particle		3.80	4.40	0.58	3.22
Single-particle		2.62	8.03	1.20	8.05
	E	3.43	3.34	0.79	3.63
Ring[a]	F	2.55	1.72	0.59	1.86
	G	2.55	1.72	0.59	1.86
Total		9.05	7.43	2.06	8.20

[a] See Fig. 3.
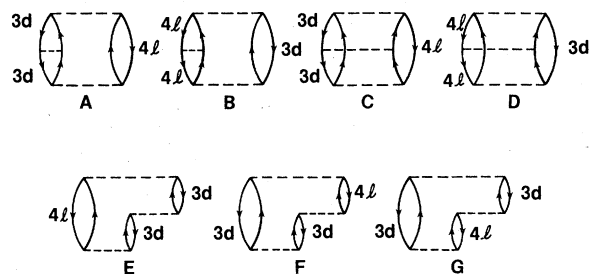
FIG. 3.   Hole-particle and ring diagrams tabulated in Tables IV and V.

appreciably for a given state of the two ions, only the division into second and higher orders. Although the second-order $4s$ energy is slightly higher for Kr VIII, the final result is smaller than that of Mo XIV because of smaller third-order effects. The rate of convergence of the perturbation expansion would thus seem to increase with increasing nuclear charge.

For nth-order diagrams, we have found that n-body interactions dominate the correlation-energy contributions. Thus, the convergence of the perturbation series is a measure of the "many-bodiness" of the system, or the complexity of the interelectronic interaction. In the present case, as the nuclear charge (a single independent-particle potential) increases, it tends to dominate the (many-particle) interelectronic interaction, making the independent particle (zeroth order) and two-particle (second and parts of higher orders) descriptions of the atom more accurate.

It was found in the calculation of these third-order effects that the off-diagonal diagrams were at least as important as the diagonal diagrams when sums over all particle lines were carried out. Thus, approximations for third-order diagrams based on summing only diagonal inter-

mediate states would yield poor results.

We were unable to devise a reliable method of estimating the off-diagonal contribution, which in some cases may be of opposite sign to the diagonal contribution, producing a cancellation in their sum.

In order to make the calculations manageable, very restricted basis sets were used in the third-order calculations. For each virtual-state symmetry, three bound and seven continuum orbitals were used to compute matrix elements and construct sums corresponding to the diagrams. Bound states of higher principal quantum numbers were included through an extrapolation scheme described by Kelly.[8] Continuum matrix elements were computed numerically. The continuum energy range was chosen to map the region where the matrix elements were found to be largest in the second-order calculation. Because of the large summations and inherent cancellations involved in computing these diagrams, these sums are expected to be less accurate than those of second order. (A second-order calculation performed for Mo XIV $4p$ with both the full and the restricted basis sets, however, gave results within a few percent of one another.)

In Table VI we list the final values for the $3l$-$4s$, -$4p$ correlation energies of Kr VIII and Mo XIV including all second-order diagrams and major third-order diagrams. It is clear that consideration of third-order diagrams is essential if adequate convergence of the perturbation series is to be assured. Table VII compares ionization energies obtained from the Hartree-Fock method,[11] many-body perturbation theory (MBPT) (present), MCHF (Froese-Fischer),[12] and the estimated experimental values where the relativistic shifts were subtracted. Good agreement is observed between the MBPT, MCHF, and observed values for Kr VIII, and between the MBPT and observed va-

TABLE V. $4p$ third-order correlation energies ($\times 10^{-3}$ a.u.).

Diagram		Kr VIII		Mo XIV	
		$3d4p \rightarrow kdk'p$	$3d4p \rightarrow kfk's$	$3d4p \rightarrow kdk'p$	$3d4p \rightarrow kfk's$
Hole-hole		0.96	1.16	0.33	0.78
	A	−1.81	−3.27	−0.62	−1.49
Hole-particle[a]	B	−1.22	−2.20	−0.40	−1.05
	C	−2.15	−2.11	−0.77	−1.03
	D	−1.39	−1.40	−0.52	−0.73
Particle-particle		3.18	4.54	1.08	1.27
Single-particle		0.49	0.90	0.24	0.56
	E	3.74	2.59	0.94	1.21
Ring[a]	F	2.54	1.33	0.73	0.60
	G	2.54	1.33	0.73	0.60
Total		6.88	2.87	1.74	0.72

[a] See Fig. 3.

TABLE VI. MBPT $3l4l'$ correlation energies ($\times 10^{-3}$ a.u.).

Order	Kr VIII		Mo XIV	
	$4s$	$4p$	$4s$	$4p$
Second	−60.8	−44.2	−56.4	−28.4
Third	16.5	9.8	10.3	2.5
Total	−44.3	−34.5	−46.1	−25.9

lues for Mo XIV.

IV. MULTIPLET STRENGTHS

The line strength for a dipole transition between an initial state Ψ_i and a final state Ψ_f is given by[13]

$$S = |\langle \Psi_i |D| \Psi_f \rangle|^2 , \tag{30}$$

where D is the dipole operator

$$D = \sum_{k=1}^{N_T} \vec{r} . \tag{31}$$

In the correlated case, we may write the $1s^2 \cdots 3d^{10}4s$ and $1s^2 \cdots 3d^{10}4p$ wave functions as the sum of the Hartree-Fock function and a "correlation" component

$$\Psi_{4s} = \Psi_{4s}^{HF} + \chi_{4s}$$

and

$$\Psi_{4p} = \Psi_{4p}^{HF} + \chi_{4p} . \tag{32}$$

The dipole matrix element is then

$$\langle \Psi_{4s} |\vec{r}| \Psi_{4p} \rangle = \langle \Psi_{4s}^{HF} |\vec{r}| \Psi_{4p}^{HF} \rangle + \langle \chi_{4s} |\vec{r}| \Psi_{4p}^{HF} \rangle$$
$$+ \langle \Psi_{4s}^{HF} |\vec{r}| \chi_{4p} \rangle + \langle \chi_{4s} |\vec{r}| \chi_{4p} \rangle . \tag{33}$$

If χ is taken as the first-order correction to the Hartree-Fock wave function involving correlation between the $4l$ electron and $n = 3$ core states, then

$$\chi_{4l} = \chi_{3s4l} + \chi_{3p4l} + \chi_{3d4l} , \tag{34}$$

where $\chi_{3l4l'}$ represents the correction to the zeroth-order function, Ψ^{HF}, due to correlation between the $4l'$ electron and the $3l$ subshell. A typical diagram is shown in Fig. 4(a).

TABLE VII. Comparison of MBPT ionization energies with other sources.

	Kr VIII		Mo XIV	
	$4s$	$4p$	$4s$	$4p$
Hartree-Fock	4.514	3.883	10.869	9.837
MBPT	4.558	3.918	10.915	9.863
MCHF[a]	4.560	3.914		
I_{obs}^{nonrel}	4.556	3.927	10.915	9.876

[a] See Ref. 12.
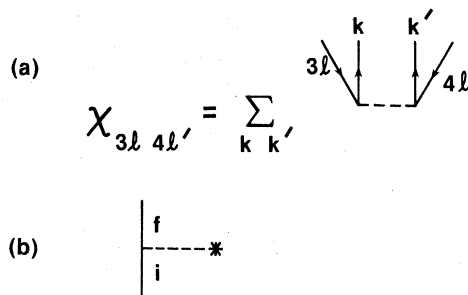
FIG. 4. (a) First-order correction to the Hartree-Fock wave function involving correlation between the $4l'$ electron and a $3l$ core state. (b) Diagrammatic representation of the dipole matrix element.

The last term in Eq. (33) represents transitions between virtual excitations. For the first-order corrections illustrated in Fig. 4(a), $\langle \chi_{4s} |\vec{r}| \chi_{4p} \rangle$ has the form

$$\sum \frac{\langle ab|v|cd \rangle}{d} \langle e|\vec{r}|f \rangle \frac{\langle gh|v|ij \rangle}{d} . \tag{35}$$

The additional matrix element over denominator causes these terms to be small compared to those involving a Hartree-Fock hole wave function and a correlation component. They have been neglected in the present calculation.

The diagram corresponding to the dipole matrix element $\langle i|\vec{r}|f \rangle$ is shown in Fig. 4(b). Note that in this case, f is not necessarily a virtual excitation, even though it is directed upward. It may also be a Hartree-Fock hole line corresponding to the *physical* excited state. (In the zeroth-order case both i and f are Hartree-Fock functions.) Thus, the Goldstone convention for labeling hole and particle lines is not rigidly adhered to in dipole integral correlation diagrams.

Diagrams corresponding to all nonzero first-order corrections to the dipole matrix element are shown in Fig. 5. Diagrams 5(I) and 5(II) represent correlation in the $4s$ initial state, and diagrams 5(III) and 5(IV) represent correlation in the $4p$ final state. A list of all possible excitations associated with these first order diagrams is given in Table VIII. Note that the excitation symmetries involved in each class of diagrams are limited by the angular momentum selection rules of the dipole interaction. Since the final-state wave function is required to have occupied $3l$ and $4p$ states, many otherwise large Coulomb matrix elements are eliminated. The factor in brackets in Fig. 5 is a normalization correction. The present formulation of the line strength assumes normalized total wave functions, whereas in the perturbation theory each occupied and virtual orbital is individually normalized.

$$= \sum_k \frac{<3\ell\; 4s\,|\mathit{v}|\,4pk>}{\epsilon_{3\ell}+\epsilon_{4s}-\epsilon_{4p}-\epsilon_k}\; <k|\vec{r}|3\ell>$$

$$= \sum_k \frac{<3\ell\; 4s\,|\mathit{v}|\,k4p>}{\epsilon_{3\ell}+\epsilon_{4s}-\epsilon_k-\epsilon_{4p}}\; <k|\vec{r}|3\ell>$$

$$= \sum_k <3\ell|\vec{r}|k>\; \frac{<k\,4s\,|\mathit{v}|\,4p\,3\ell>}{\epsilon_{4p}+\epsilon_{3\ell}-\epsilon_k-\epsilon_{4s}}$$

$$= \sum_k <3\ell\,|\vec{r}|k>\; \frac{<4s\,k\,|\mathit{v}|\,4p\,3\ell>}{\epsilon_{4p}+\epsilon_{3\ell}-\epsilon_k-\epsilon_{4s}}$$

$$<\psi_{4s}|\vec{r}|\psi_{4p}> = [\,\eta\,]^{-1}\left\{ <\psi_{4s}^{HF}|\vec{r}|\psi_{4p}^{HF}> + I + II + III + IV \right\}$$

FIG. 5. Correlation diagrams for the line strength.

TABLE VIII. Angular momentum combinations for virtual excitations occurring in Fig. 5.

Class	Diagram	Core state	Excitation symmetry
I	A	$3d$	p
I	B	$3d$	f
II	C	$3d$	p
II	D	$3d$	f
I	E	$3p$	s
I	F	$3p$	d
II	G	$3p$	s
II	H	$3p$	d
I	I	$3s$	p
II	J	$3s$	p
III	K	$3d$	p
III	L	$3p$	s
III	M	$3s$	p
IV	N	$3d$	p
IV	O	$3d$	f
IV	P	$3p$	s
IV	Q	$3p$	d
IV	R	$3s$	p
III	S	$3d$	f
III	T	$3p$	d

Correlation corrections to the transition integral were computed using the same virtual basis sets as the correlation energy calculation. The results are given in Tables IX and X. Table IX lists the correlation contributions to the transition integral where correlation in the 4s state is considered and also lists similar data for the 4p-state correlation. Table X summarizes the correlation contributions to the transition integral, and gives the resulting multiplet strengths.

The dominant excitation contributing to the 4s-4p multiplet strength correlation was found to be $3d4s \rightarrow kf4p$ (diagrams D and O in Table VIII), which was also the most important one for the ground-state ionization energy calculation. Because of the dipole selection rules, the excitation pair $3d4p \rightarrow kdk'p$, important in the 4p correlation energy, does not contribute. Cancellation between contributions to the dipole matrix element of opposite sign was observed, with the final correlation component being approximately equal to the sum of diagrams D and O. For correlations in the 4s initial state, the general pattern is for the absolute magnitudes of the diagrams to decrease as the ionic charge increases. For the 4p final-state correlations, the major contribution decreases (diagram O in Table VIII), but lesser diagrams increase. In all cases, the normalization corrections were found to be small. In Kr VIII, the final normalization correction was 1.007, in Mo XIV it was 1.005.

The present calculation yields multiplet strengths in excellent agreement with the multiconfiguration Hartree-Fock results of Froese-Fischer.[12] Exact agreement is not expected due to the ambiguity between two- and three-electron contributions in the MCHF data, as well as the contrasting theoretical formalisms. The present calculation is limited to two-body correlation effects in initial and final states, with sums over all possible excitations. In the MCHF calculation, the $3d^{10}$ core was partially relaxed so that the final 3d wave function was allowed to differ from that of the other nine, producing a $3d^9 3d'\;^1S$ core instead of a $3d^{10}\;^1S$, in which all 3d wave functions are the same. Such a core relaxation would correspond to three-body effects in a perturbation series. The difference in theoretical methods should be more apparent in the neutral end of the sequence, where correlation effects are most pronounced.

A useful quantity in astrophysics and plasma physics is the oscillator strength f defined as[14]

$$f = \tfrac{2}{3}(\Delta E/g)S. \tag{36}$$

A comparison of theoretical and experimental f-values for the Cu–I isoelectronic sequence is shown in Fig. 6. Clearly, there is a large systematic discrepancy between the best theoretical calculations and beam-foil experimental data for ions heavier than zinc. This large disparity is surprising for a system with only a single valence electron outside a closed-shell core with different principal quantum numbers and was a motivation for the present work. Although inclusion of cor-

TABLE IX. Correlation corrections to the radial dipole matrix element due to first-order correlations in the $4l$ wave function ($\times 10^{-3}$ a.u.).[a]

| | 4s correlation | | | 4p correlation | |
Diagram	Kr VIII	Mo XIV	Diagram	Kr VIII	Mo XIV
A	−0.935	−0.139	K	−1.504	−1.362
B	−1.021	−0.906	L	−1.709	−1.524
C	−1.814	−0.214	M	0.047	0.017
D	−15.71	−9.097	N	−3.022	−0.730
E	0.210	0.138	O	−26.74	−14.68
F	−0.119	−0.111	P	−0.147	−0.100
G	−0.829	−1.224	Q	−1.732	−1.274
H	−0.130	−0.061	R	−0.091	−0.081
I	0.043	0.036	S	−1.665	−1.154
J	−0.199	−0.164	T	0.024	0.017
Total	−20.50	−11.74	Total	−36.54	−19.87

[a] The Hartree-Fock integral is positive.

relation effects does reduce the Hartree-Fock values somewhat, especially at the neutral end, there still remains a (10–20)% systematic discrepancy which does not appear to be explained by higher-order theoretical effects. The excellent agreement between Froese-Fischer's MCHF data[12] and the present MBPT values, obtained by quite different theoretical formalisms, is a strong indication that the theoretical multiplet strengths have converged.

It is highly unlikely that the problem has its origin in relativistic effects on the radial wave functions. Younger and Weiss[15] have studied the limiting case of the hydrogen isoelectronic sequence using exact solutions of the Dirac equation for a particle in a Coulomb field. Deviations of the line strengths from nonrelativistic values rarely amount to more than a few percent at $Z = 50$, and in no case do they change the nonrelativistic f by the 30% that would be required in the Cu–I sequence. In many electron atoms, relativistic effects will be less serious than in the hydrogenic case due to the screening effects by the other electrons.

TABLE X. MBPT transition integrals and multiplet strengths.

		Kr VIII	Mo XIV
Radial Matrix Element	Hartree-Fock[a]	0.813	0.579
	4s correlation	−0.021	−0.012
	4p correlation	−0.037	−0.020
	Total	0.755	0.547
Normalization		1.007	1.005
Multiplet Strength	Hartree-Fock[a]	3.96	2.01
	MBPT	3.37	1.78
	MCHF[b]	3.40	1.82

[a] See Ref. 11.
[b] See Ref. 12.

Younger and Weiss[15] have found that an excellent approximation to the Dirac-Hartree-Fock line strength may be obtained by multiplying the nonrelativistic value by the ratio

$$C_R = S_{H_{rel}}(Z)/S_{H\,nonrel}(Z) , \qquad (37)$$

where $S_{H_{rel}}$ is the hydrogenic relativistic line strength and $S_{H\,nonrel}$ is the nonrelativistic value. The charge is the full and not screened charge of the nucleus. For Kr VIII and Mo XIV these correction factors are 0.978 and 0.970, respectively, producing "relativistic" multiplet strengths of 3.66 (Kr VIII) and 1.78 (Mo XIV).

An explanation of the continuing discrepancy has been proposed by Younger and Wiese[6] in an extensive discussion of the beam-foil method for determining lifetimes. It is well known that, following
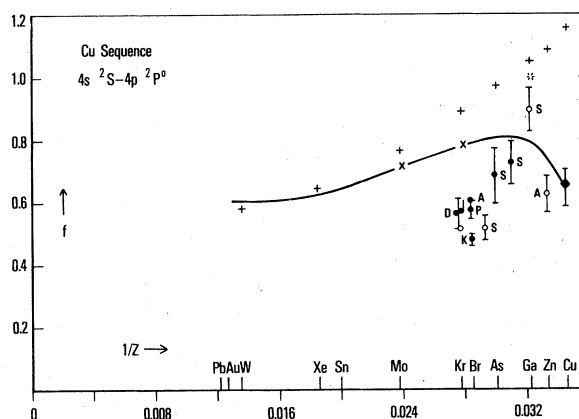
FIG. 6. Systematic trend for the oscillator strength of the $4s\,^2S - 4p\,^2P$ resonance transition of the Cu isoelectronic sequence: ♦, critical compilation (Ref. 18); ●, beam-foil data: P, Ref. 19; K, Ref. 20; I, Ref. 21; D, Ref. 16; A, Ref. 22; S, Ref. 17; A', Ref. 23; +, HF, (Ref. 11); solid curve, MCHF (Ref. 12); *, semiempirical (Ref. 24); ×, MBPT (present).

excitation by the foil, many excited states other than the one being monitored are populated. Some of these states may decay directly or indirectly into the primary level, repopulating it and altering the shape of the decay curve from that of a single exponential. These "cascades" are usually accounted for by decomposing the decay curve into two or three exponential decay components. One of these, the primary, corresponds to the state under study, and the remaining one or two account for the repopulating cascades. It has been shown, however, that the number of exponentials involved in the actual decay may number ten or more, and that unless adequate attention is paid to all of them, an erroneous primary lifetime will result. There is a subtle masking occurring, so that while the curve may *appear* to be a single exponential, it may *actually* be a 30-exponential curve constructed from lifetimes quite different from those extracted from a two- or three-exponential fit.

Based on atomic-structure considerations, they propose that the disagreement between the theoretical and experimental lifetimes and multiplet strengths is due to the presence of these many repopulating cascades, and that the decomposition of an experimental curve into two or three exponentials is insufficient to extract the true primary lifetime.

V. SUMMARY

Many-body diagrammatic perturbation theory has been applied to the calculation of ionization energies and line strengths for two highly ionized members of the copper isoelectronic sequence. The close agreement between MCHF and MBPT line strengths support the conclusions of Younger and Wiese[6] that the reason for the continued discrepancy between theoretical and beam-foil experimental data in the Cu sequence is primarily experimental in origin, and not due to the neglect of correlation effects.

ACKNOWLEDGMENTS

APPENDIX: EXAMPLE OF A UNIFIED HAMILTONIAN FOR THE $1s^2 2s$ CONFIGURATION

As an example of a unified Hamiltonian we consider the ground state of a lithiumlike atom:

$1s^2 2s$. In this case there is only one closed-shell orbital, ϕ_{1s}, and one open-shell orbital, ϕ_{2s}. The Hartree-Fock equations for ϕ_{1s} and ϕ_{2s} are

$$F_{1s}\phi_{1s} = (t + 2J_{1s} - K_{1s} + J_{2s} - \tfrac{1}{2}K_{2s})\phi_{1s}$$
$$= \epsilon_{11}\phi_{1s} + \epsilon_{12}\phi_{2s} \tag{A1}$$

and

$$F_{2s}\phi_{2s} = (t + 2J_{1s} - K_{1s})\phi_{2s} = 2\epsilon_{21}\phi_{1s} + \epsilon_{22}\phi_{2s}, \tag{A2}$$

where $\epsilon_{12} = \epsilon_{21}$ is the off-diagonal Lagrangian multiplier necessary to ensure orthogonality between ϕ_{1s} and ϕ_{2s}. It is a simple matter to show that

$$\epsilon_{12} = -\langle \phi_{2s} | J_{2s} - \tfrac{1}{2}K_{2s} | \phi_{1s} \rangle. \tag{A3}$$

Following Roothaan, we replace the off-diagonal terms with coupling operators

$$2L_0 = |\phi_{2s}\rangle\langle\phi_{2s}|\tfrac{1}{2}J_{2s} + \tfrac{1}{2}J_{2s}|\phi_{2s}\rangle\langle\phi_{2s}|,$$
$$L_c = |\phi_{1s}\rangle\langle\phi_{1s}|\tfrac{1}{2}J_{2s} + \tfrac{1}{2}J_{2s}|\phi_{1s}\rangle\langle\phi_{1s}|,$$
$$2M_0 = |\phi_{2s}\rangle\langle\phi_{2s}|\tfrac{1}{2}K_{2s} + \tfrac{1}{2}K_{2s}|\phi_{2s}\rangle\langle\phi_{2s}|,$$
$$M_c = |\phi_{1s}\rangle\langle\phi_{1s}|\tfrac{1}{2}K_{2s} + \tfrac{1}{2}K_{2s}|\phi_{1s}\rangle\langle\phi_{1s}|, \tag{A4}$$

so that the pseudoeigenvalue equations (A1) and (A2) become

$$F_c\phi_{1s} = \epsilon_{11}\phi_{1s} \tag{A5}$$

and

$$F_0\phi_{2s} = \epsilon_{22}\phi_{2s} \tag{A6}$$

where the open- and closed-shell Fock operators F_0 and F_c are

$$F_c = t + 2J_{1s} - K_{1s} + J_{2s} - \tfrac{1}{2}K_{2s} + 4L_0 - 2M_0 \tag{A7}$$

and

$$F_0 = t + 2J_{1s} - K_{1s} + 4L_c - 2M_c. \tag{A8}$$

We now define a *unified* Fock operator F as

$$F = t + 2J_{1s} - K_{1s} - (J_{2s} - \tfrac{1}{2}K_{2s}) + 2(2L_c - M_c)$$
$$+ 2(2L_0 - M_0) \tag{A9}$$

Direct calculation verifies that

$$F\phi_{1s} = \eta_1\phi_{1s}, \tag{A10}$$
$$F\phi_{2s} = \eta_2\phi_{2s}, \tag{A11}$$

where

$$\eta_1 = \epsilon_{11} + \langle\phi_{1s}|2J_{2s} - K_{2s}|\phi_{1s}\rangle, \tag{A12}$$
$$\eta_2 = \epsilon_{22} + \langle\phi_{2s}|J_{2s} - \tfrac{1}{2}K_{2s}|\phi_{2s}\rangle, \tag{A13}$$

which are the same equations as if one had applied Eq. (5) directly.

[1] E. Hinnov, Princeton Plasma Physics Laboratory Report No. MATT-1024, 1974 (unpublished).

[2] E. Hinnov, Princeton Plasma Physics Laboratory Report No. MATT-1022 (unpublished).

[3] W. L. Wiese and S. M. Younger, in *Beam Foil Spectroscopy*, edited by I. A. Sellin and D. J. Pegg (Plenum, New York, 1976).

[4] L. J. Curtis, *Beam Foil Spectroscopy*, edited by S. Bashkin (Springer-Verlag, Berlin, 1976), p. 63.

[5] C. Laughlin and A. Dalgarno, Phys. Rev. A 8, 39 (1973).

[6] S. M. Younger and W. L. Wiese, Phys. Rev. A 17, 1944 (1978).

[7] J. Goldstone, Proc. R. Soc. Lond. 239, 267 (1957).

[8] H. P. Kelly, Adv. Chem. Phys. 14, 129 (1969).

[9] C. C. J. Roothaan, Rev. Mod. Phys. 32, 179 (1960).

[10] J. Reader (private communication).

[11] A. W. Weiss (private communication).

[12] C. Froese-Fischer, J. Phys. B 10, 1241 (1977).

[13] I. B. Levinson and A. A. Nikitin, *Handbook for Theoretical Computation of Line Intensities in Atomic Spectra* (Danial Davey, New York, 1965).

[14] C. W. Allen, *Astrophysical Quantities* (Athlone, London, 1955).

[15] S. M. Younger and A. W. Weiss, J. Res. Natl. Bur. Stand. A 79, 629 (1975).

[16] M. Druetta and J. P. Buchet, J. Opt. Soc. Am. 66, 433 (1976).

[17] G. Sorensen, Phys. Rev. A 7, 85 (1973).

[18] T. M. Bieniewski and T. K. Krueger, Aerospace Radiation Laboratory Report No. ARL 71-0135, Project No. 7114, 1974 (unpublished).

[19] E. H. Pinnington, J. A. Kernahan, and K. E. Donnelly, J. Opt. Soc. Am. 67, 162 (1977).

[20] E. J. Knystautas and D. Drouin, J. Quant. Spectrosc. Radiat. Transfer 17, 551 (1977).

[21] D. J. G. Irwin, J. A. Kernahan, E. H. Pinnington, and A. E. Livingston, J. Opt. Soc. Am. 66, 1396 (1976).

[22] T. Andersen and G. Sorensen, J. Quant. Spectrosc. Radiat. Transfer 13, 369 (1973).

[23] T. Andersen, A. K. Nielsen, and G. Sorensen, Nucl. Instrum. Methods 110, 143 (1973).

[24] J. Migdalek, Can. J. Phys. 54, 130 (1976).